JOURNAL OF PROPULSION AND POWER
Vol. 26, No. 4, July–August 2010

Film Effectiveness Measurements on the Pressure Surface of a Transonic Airfoil

Paul M. Kodzwa Jr.* and John K. Eaton†
Stanford University, Stanford, California 94305

DOI: 10.2514/1.46668

This paper presents steady-state film effectiveness measurements for two rows of compound-angle round holes on the pressure surface of a modern, highly cambered, transonic airfoil. A single-passage model was used to simulate the idealized two-dimensional flowpath between rotor blades in a modern transonic turbine. This setup offered a simpler construction than a linear cascade, yet produced an equivalent flow condition. Validated high-accuracy (±0.2°C) surface-temperature measurements were performed using wideband thermochromic liquid crystals, allowing direct measurement of the adiabatic cooled-wall temperature. The peak Mach number along the pressure surface was 1.5 and maximum turbulence intensity was 30%. To simulate the effect of temperature gradients on coolant behavior, carbon dioxide and air were used as the injectant. The data indicate that jet blowoff appears to occur at blowing rates that are significantly higher than previously observed. Furthermore, the data suggest that increasing injectant density only improves effectiveness when the coolant jets are attached to the surface. It was observed that at high turbulence levels, the attached coolant jets degrade faster and jet blowoff is suppressed as blowing rates are increased.

Nomenclature

$A_{c,j}$	=	cross-sectional area of film cooling hole, m^2
Bi	=	Biot number, $h\mathcal{P}/k$
BL	=	blowing or mass flux ratio, $\rho_j u_j/\rho_\infty u_\infty$
c_{blade}	=	blade chord length, mm
c_p	=	specific heat with constant pressure
c_v	=	specific heat with constant volume
D	=	film cooling plenum internal diameter, mm
DR	=	density ratio, ρ_j/ρ_∞
d	=	pinned film cooling hole diameter, mm
H_{model}	=	model height, mm
h	=	heat transfer coefficient, $W/(m^2 \cdot K)$
I	=	momentum flux ratio, $\rho_j u_j^2/\rho_\infty u_\infty^2$
K_∞	=	acceleration parameter, $[\nu(T_{\circ,\infty})/u_\infty^2](du_\infty/d\lvert s_c\rvert)$
k	=	thermal conductivity, $W/(m \cdot K)$
L	=	film cooling hole length, mm
ℓ	=	integral length scale, mm
M	=	Mach number, $u_\infty/\gamma RT$
M_{is}	=	isentropic Mach number
$\dot{m}$	=	mass flow rate, kg/s
$N_{c,j}$	=	number of cooling holes
q''	=	surface heat flux, $kW/(m^2 \cdot K)$
$\mathcal{P}$	=	perpendicular distance, mm
P	=	static pressure, Pa
Pr	=	Prandtl number $\mu c_p/k$
$P_\circ$	=	stagnation (total) pressure, Pa
p	=	film cooling hole pitch spacing, mm
r_∞	=	recovery factor
R_∞	=	air gas constant, $J/(kg \cdot K)$
Re_c	=	chord Reynolds number, $\rho\tilde{u}_{\text{inlet}} c_{\text{blade}}/\mu$
Re_k	=	roughness Reynolds number
s_c	=	distance relative to stagnation point along airfoil surface, mm
T	=	static temperature, °C
TI%	=	turbulence intensity
$T_\circ$	=	stagnation (total) temperature, °C
u_∞	=	freestream velocity
Z'	=	dimensionless spanwise surface coordinate relative to the centerline of the passage
z	=	spanwise surface coordinate relative to the centerline of the passage, mm
α	=	angle of hole inclination relative to surface tangent, deg
β	=	angle of hole rotation relative to axial direction, deg
δ	=	uncertainty
η	=	film effectiveness, $(T_c - T_{\text{ref}})/(T_{w_2} - T_{\text{ref}})$
η_T	=	film effectiveness based on total temperature, $(T_c - T_{\text{rec}})/(T_{\circ,j} - T_{\text{ref}})$
γ	=	ratio of specific heats, c_p/c_v
ν	=	kinematic viscosity, m^2/s
ρ	=	density, kg^3/m

Subscripts

blade	=	blade dimensions
c	=	blade surface, cooled condition
is	=	isentropic condition
j	=	film cooling jet condition
$\circ$	=	stagnation (total) condition
rec	=	recovery condition
T	=	total temperature
TLC	=	liquid-crystal-measured temperature
$w2$	=	hole exit condition
1	=	row 1
2	=	row 2
∞	=	mainstream condition
$'$	=	refers to dimensionless distance

Received 15 August 2009; revision received 9 March 2010; accepted for publication 22 March 2010.

*Research Assistant. Senior Member AIAA.
†Professor. Senior Member AIAA.

I. Introduction

RESEARCHERS have directed tremendous effort toward the design of advanced cooling strategies for gas turbine engine applications. Effective cooling of high-temperature engine components allows higher turbine inlet temperatures and improved engine performance. A typical approach is to eject a lower-temperature fluid through a series of discrete holes that are strategically positioned to ensure adequate coverage. Ideally, low-temperature fluid forms a film that reduces the surface heat flux to

the component. This technique is called *film cooling*. Despite the simplicity of the film cooling concept, massive effort is required to optimize coolant hole shapes, locations and flow rates for a given component. This reality is due to the wide variety of mainstream flow parameters that affect film cooling performance, any of which may dominate under differing circumstances. Furthermore, there have been documented difficulties predicting film cooling performance at conditions relevant to modern turbomachinery design [1]. Generically, on a typical rotor blade airfoil, designers place varying-geometry film cooling holes near the leading edge and midchord and place shaped slots at the airfoil trailing edge. One parameter used to characterize film cooling performance is the *film cooling effectiveness* η and is defined as

$$\eta = \frac{T_c - T_{\text{ref}}}{T_{w_2} - T_{\text{ref}}} \tag{1}$$

where T_c is the temperature measured on an adiabatic surface where the stagnation temperature of the coolant is above or below the stagnation temperature of the mainstream flow ($T_{\circ,j} \neq T_{\circ,\infty}$). T_{w_2} represents the coolant temperature at the exit of the film cooling hole and T_{ref} is the reference temperature at which the surface is adiabatic. For incompressible flows with film cooling, the reference temperature is the freestream temperature ($T_{\text{ref}} = T_\infty$). In high-speed flows, T_{ref} is defined as the *recovery temperature* ($T_{\text{ref}} = T_{\text{rec}}$) [2]. As $M_\infty \to 0$, $T_{\text{rec}} = T_\infty$. By definition, accurate measurements of η require $q'' = 0$ [3]. Full-field measurements of η have been obtained for transonic cascades using the transient narrowband liquid-crystal technique [4]. Narrowband thermochromic liquid crystals (TLCs) change colors over a very narrow temperature bandwidth (1°C or less). They are applied to a surface where q'' changes in response to transient variations of T_{w_2} to find contours of η. Wang et al. [5] and Drost et al. [6] point out that this technique requires the regression of 6 to 8 tests to achieve an estimated ±4% uncertainty ($P = 0.95$) for a nominal effectiveness value of $\eta = 0.3$ with a temperature differences of $T_c - T_{\circ,j} \approx 30$°C. Note that as $q'' \neq 0$ for this technique, η and T_{rec} cannot be directly measured.

The goal of the present work is to provide comprehensive full-field measurements of η under a wide range of conditions for a highly loaded, transonic turbine cascade with steady-state flow conditions and over a near-adiabatic surface. These data should be useful for direct comparisons to simulations, so we established well-defined flow and heat transfer boundary conditions. Surface-temperature measurements are made using the wideband TLC technique, which allows direct measurements of T_c and T_{rec} with the same heat transfer surface. These TLCs change color over a 10–15°C bandwidth. This approach allows direct measurement of η, eliminating the need for multiple tests as required for narrowband TLCs. The compromises that must be made in order to obtain this detailed data set are that the cascade is nonrotating, and both the temperature and density gradients are much lower than true engine conditions.

II. Test Apparatus and Procedures

We constructed a simplified linear cascade (a single-passage test rig) around a highly cambered blade geometry consistent with an advanced first-stage rotor blade operating at mean flow Mach numbers as high as 1.5. Haldeman et al. [7] performed full-scale rotating turbine tests for aerodynamic and heat transfer measurements with a similar geometry. Exactly the same geometry was used by Vicharelli and Eaton [8] in a two-dimensional double-passage cascade to acquire detailed turbulence measurements. Table 1 lists the experimental flow conditions that were selected to give engine representative *Reynolds* and inlet *Mach* numbers. At operation conditions, these values had expected ranges of: $3.5(10)^5 \leq Re_c \leq 8(10)^5$ and $0.2 \leq M \leq 0.4$ [9]. The film effectiveness measurements were performed on the pressure surface. All film cooling tests had absolute temperature ratios of approximately unity ($T_{\circ,j}/T_{\circ,\infty} \approx 1.0$). This raised an obvious concern with respect to modeling the substantial temperature (and by extension density) gradients present in the real film cooling problem, especially if air is the coolant.

Table 1 Experimental conditions

Parameter	Test Condition
Chord length c_{blade}, mm	36.1
Airfoil pitch spacing AP, mm	39.8
γ_{inlet}, c_v/c_p	1.4
Inlet angle	29.2°
Exit angle	−68.6°
$P_{o,\text{inlet}}/P_{\text{exit}}$	2.57
$P_{o,\text{inlet}}$, Pa	$2.60(10)^5$
$T_{o,\text{inlet}}$, K	300
Inlet Mach number	≈0.340
Reynolds number, $Re_c = \rho \tilde{u}_{\text{inlet}} c_{\text{blade}}/\mu$	$6.62(10)^5$

Nevertheless, compressible flat-plate boundary-layer experiments have showed that carbon dioxide injection produces thermal and flow conditions that are entirely analogous to those taken at engine representative conditions with air injection [10].

A. Design and Testing of Single-Passage Flow Facility

Figure 1 presents a layout of the test facility. The test rig replicated the airfoil pressure and suction surfaces along the upper and lower walls of the passage between points D and E and F and G, respectively. The bleeds upstream of the test surfaces removed the inlet boundary layers. The bleed plena shapes and flow rates were chosen to correctly position the stagnation points on the two airfoil surfaces. Kodzwa et al. [11] performed a computational optimization procedure to design the inlet and exit wall geometries to produce a flowfield that is equivalent to an infinite cascade of blades. The bleed flow exhausts were individually metered using a downstream orifice to insure consistent placement of the stagnation points and accurate replication of the flowfield between tests. The bleed mass flow rates had an estimated uncertainty of less than 8% ($P = 0.95$).

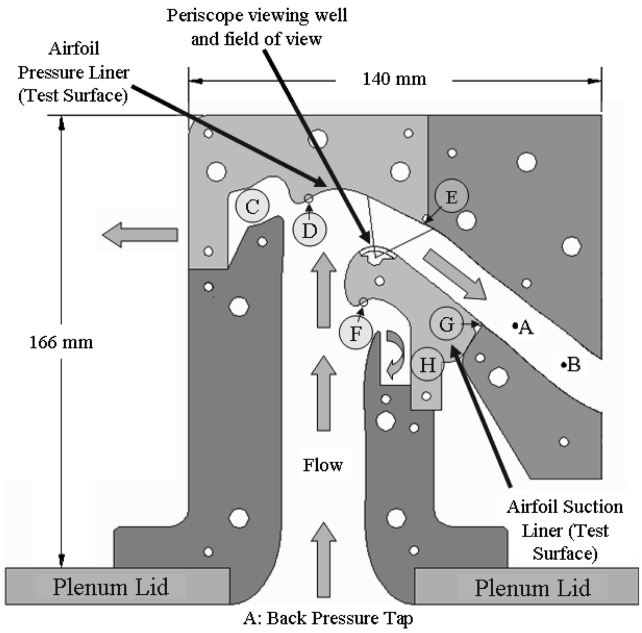

A: Back Pressure Tap

B: 1st Downstream Pressure Tap

C: Pressure Side Boundary Layer Bleed Chamber

D: Stagnation Point (Pressure)

E: Trailing Edge (Pressure)

F: Stagnation Point (Suction)

G: Trailing Edge (Suction)

H: Suction Side Boundary Layer Bleed Chamber

Fig. 1 Schematic of single-passage experiment.

The model consisted of six primary elements as indicated in Fig. 1. These measurement surfaces could be swapped out for pressure or heat transfer measurements. Each of the components has a depth of 50.8 mm and are mounted between two parallel endwalls. The model has an aspect ratio ($AR = H_{model}/AP$) of 1.276. We used a low thermal conductivity material [RenShape 450, $k = 0.2$ W/(m · K)] to fabricate all model components to minimize thermal losses. The model mounts on top of a 0.064 m^3 aluminum plenum connected to the model bellmouth. Filtered dry air fed by a screw compressor and a refrigerated dryer was supplied to the plenum via an electrically heated pipe run. We used an orifice plate to measure the flow rate to within 2% of the nominal flow rate. The underside of the plenum lid was designed to accept a removable aluminum grid, as pictured in Fig. 2. This grid was specially designed to simulate the characteristically high turbulence intensity levels of a modern turbine engine. It consisted of a series of triangular tabs spaced 19 mm apart in both directions. To estimate the turbulence conditions approximately 1.2 axial chord lengths (c_{blade}) upstream, we performed single hot-wire measurements. As the flow at this location was indeed compressible, our approach only allowed the measurement of the mean and fluctuating streamwise mass flux in order to estimate the local turbulence intensity TI%. Note that this measurement has the implied assumption of local isotropy. Furthermore, we assumed the validity of Taylor's hypothesis on fluctuating mass flux data to estimate the integral length scale ℓ. Note that Taylor's hypothesis requires both the assumption of local isotropy and small fluctuating velocities ($u'/u_\infty \ll 1$). Our measurements indicated that without the grid, TI% = 1.5% and $\ell/c_{blade} = 0.53^{+0.5}_{-0.4}$. In contrast, with the grid, we measure TI% = 30%. We do not report ℓ for the high-turbulence case as TI% definitely was outside the valid application range for Taylor's hypothesis. Note that TI% = 30% is considerably higher than in previous investigations [4,12,13]. Furthermore, Vicharelli and Eaton [8], using the same turbulence grid, report no change in inlet turbulence quantities from inlet to the blade leading edge for the two-passage version of this experiment. This report also suggests an integral length scale of $\ell/c_{blade} = 0.16^{+0.08}_{-0.08}$ for the high-turbulence condition. As the single-passage model has identical mean flow conditions, we expect that TI% $\approx$ 30% at the blade leading edge in this experiment as well.

Kodzwa et al. [11] also performed three-dimensional numerical simulations of the experimental facility for design and evaluation purposes. An examination of the M_{is} distributions at various spanwise locations ($Z' = z/H_{model}$) revealed that the two-dimensional portion of the flow was in the range $-0.25 \le Z' \le 0.25$. By definition, $Z' = 0$ at the centerline of the passage.

Static pressure measurements were collected on airfoil pressure and suction surfaces with closely spaced, 0.62-mm-diam pressure taps installed along the centerline of the passage. The measured pressure distributions were expressed as an *isentropic Mach number* M_{is}, using standard isentropic flow functions.

Figure 3 compares the measured M_{is} distributions at low- and high-turbulence conditions to the computed M_{is} distribution for the given airfoil geometry in an infinite two-dimensional linear cascade. This figure shows close agreement between measurements and the desired pressure distribution in both cases. The one exception to this observation is at the stagnation point at the high-turbulence condition. The pressure measurements at the expected stagnation point locations read significantly lower than the estimated total pressure. This effect appears to decay rapidly along both blade surfaces. We confirmed that this discrepancy was caused by significant variations in the upstream total pressure with the grid installed via upstream total pressure measurements at the same location as our hot-wire measurements ($1.2c_{blade}$ upstream). We estimated that the M_{is} data presented in this figure have an uncertainty of approximately $\pm 7\%$. We found that the computed pressure distribution was practically identical for both high- and low-turbulence cases. This fact can be attributed to our use of a two-layer,

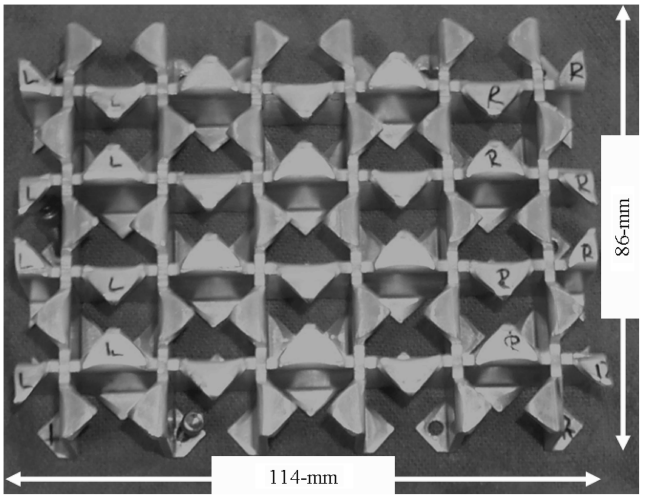

Fig. 2 Grid used to produce high-turbulence condition.

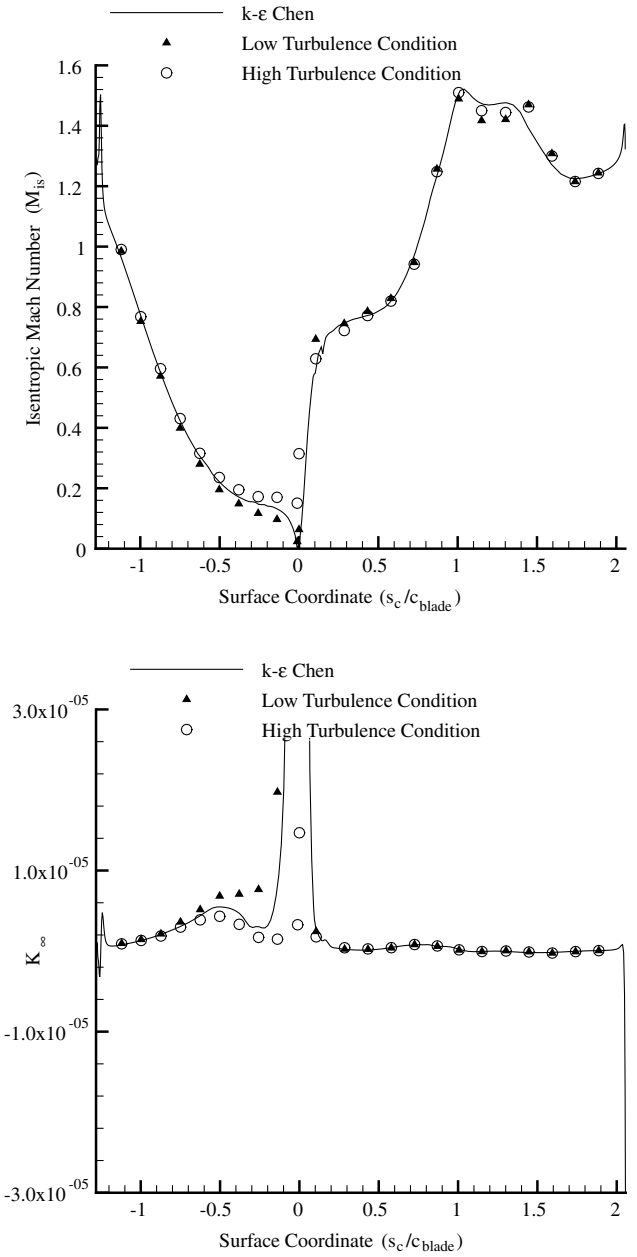

Fig. 3 Measurements of M_{is} and K_∞ compared to infinite cascade standard for low- and high-turbulence conditions.

two-equation k-ε turbulence model that incorporated a modification that imposed limiters on the production of turbulent kinetic energy [14]. The good agreement between computed and experimental pressure distributions allowed us to use the computed M_{is} distribution as an interpolating function for our data. Note that the peak M_{is} on the pressure surface is $M_{is} = 1.5$, which is considerably higher than in previous experiments. It is important to note that the good agreement between numerical predictions and experimental data indicates that the model faithfully captures the previously discussed shock structure.

We computed the acceleration factor K_∞ along the airfoil pressure surface to quantify the freestream acceleration around the blade geometry. Note that distances relative to the stagnation point along the pressure surface have a negative coordinate in Fig. 3. Since M_{is} increases monotonically along the pressure surface, K_∞ is always positive. This parameter was found to vary between $1(10)^{-6} \leq K_\infty \leq 1(10)^{-5}$ over the majority of the surface, as shown in Fig. 3. Near the stagnation point and along the aft portion of the airfoil, the numerically predicted values for K_∞ fall below the critical value for relaminarization: $K_\infty \leq 3.0(10)^{-6}$ [15]. However, using laminar predictions for T_{rec} and the heat transfer coefficient along the pressure surface, we postulated that boundary layer was likely fully turbulent [16].

B. Liquid-Crystal Periscope Thermography System

Wideband ($25°C \leq T \leq 38°C$) liquid-crystal thermography was used to obtain high-resolution T_{rec} and T_c maps. We used two miniature periscopes to image and illuminate the test surface. The periscopes were inserted into a *viewing well* installed in a modified suction surface, as shown in Fig. 1. This consisted of a round hole and a groove cut into the blade shape of the surface. A thin precision-machined and polished Plexiglas window with an outer surface that matched the removed portion of the blade shape was glued into the groove. The imaging periscope mirror reflected the image into a borescope with a set of rod lenses attached to a camera. The mirror could be rotated, allowing the adjustment of the field of view, shown in Fig. 1, in order to collect measurements over the entire measurement surface.

We had to overcome several challenges due to the complex nature of the imaging system and the inherent properties of wideband TLCs. This included the strong optical distortion effects along the path length between the borescope optics and the Plexiglas window. Furthermore, TLCs are sensitive to lighting and viewing angle in addition to temperature. To achieve high-accuracy results ($\pm 0.2°C$), it was necessary to develop an in situ calibration system that ensured repeatable thermography over the active range of the crystals. To account for the spatial distortion effects of the Plexiglas window and curved surface, a geometry calibration piece corresponding to the pressure surface was manufactured. This consisted of a RenShape piece with a closely spaced grid glued to the surface. To calibrate the liquid-crystal response, two oxygen-free, high-conductivity copper calibration pieces corresponding to the suction and pressure surfaces were constructed. The copper calibration surfaces were airbrush-painted simultaneously with the heat transfer test surfaces. We did not perform any surface roughness measurements on either painted surface. However, the TLC we used in this study consisted of a slurry of microencapsulated spheres of diameter $\mathcal{O}(10)$ μm. The approximate thickness of this layer (based on the applied paint volume) was 25 μm. Previous studies using microencapsulated narrowband TLCs report roughness values that range from 3.7 to 15 μm [4,17]. On these bases, we believe that the resulting surface roughness is of the same order. Using numerically computed values of the maximum shear stress along the pressure surface, we estimated a maximum roughness Reynolds number of $Re_k \approx 35$. The pressure-surface geometry and liquid-crystal calibration pieces were individually installed in the model and imaged through the periscope imaging system to correct for optical distortion, lighting gradients and color interpretation issues. The surfaces could be heated or cooled to within 0.1°C using a set of integral thermoelectric coolers. The heat transfer surface was then installed in the model. Each measurement surface was imaged from several overlapping fields of view that extended into the pressure-surface bleed chamber, labeled C in Fig. 1. These images were interpolated onto a single background grid. This gave a spatial resolution of $4(10)^{-3}$ mm/pixel. As we discuss in Kodzwa et al. [18] and Kodzwa and Eaton [19] each image consisted of at least 100 subregions (or cells), each with their own individual calibration curve. These calibration curves relate a color index (termed as the hue angle Q) to temperature. Over 700 cells were used to perform surface-temperature measurements. The bilinear interpolation algorithm we used to develop the single grid is discussed in Kodzwa et al. [18]. To establish that the liquid-crystal imaging system was uniformly accurate over their entire temperature range, the isothermal calibration surface was imaged at four specific temperatures that spanned the active range of the crystals. The resulting spanwise-averaged data showed that the resulting measurement uncertainty was well within desired limits ($\pm 0.1°C$). Figure 4 presents exemplary calibration curves for two cells for the first field of view; this figure also presents the spanwise-averaged temperature data with varying isothermal surface temperature. Figure 5 displays a spatially resolved temperature map derived from images of the pressure side copper calibrator at a set temperature of $T_{set} = 26.2°C$. Also shown in this figure is a picture of the painted calibrator. This contour plot along with the spanwise-averaged data confirms that the calibration process corrects for the TLC lighting/viewing angle dependency and borescope optics distortion effects.

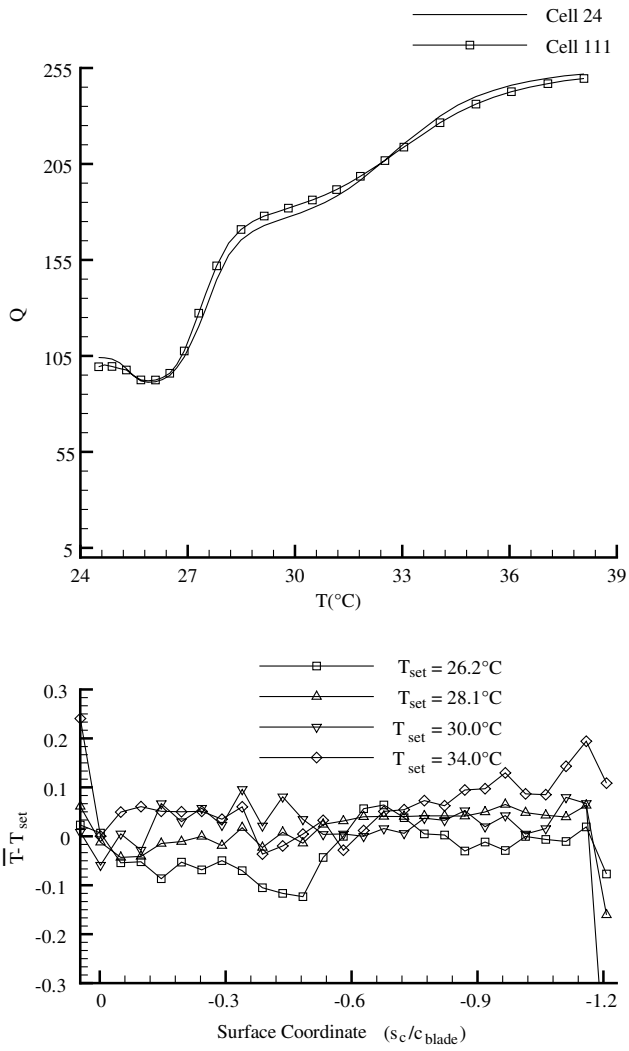

Fig. 4 Q curves for two calibration cells in zone 1 and $\bar{T} - T_{set}$ curves at $T_{set} = 26.2$, 28.1, 30.0, and 34.0°C.

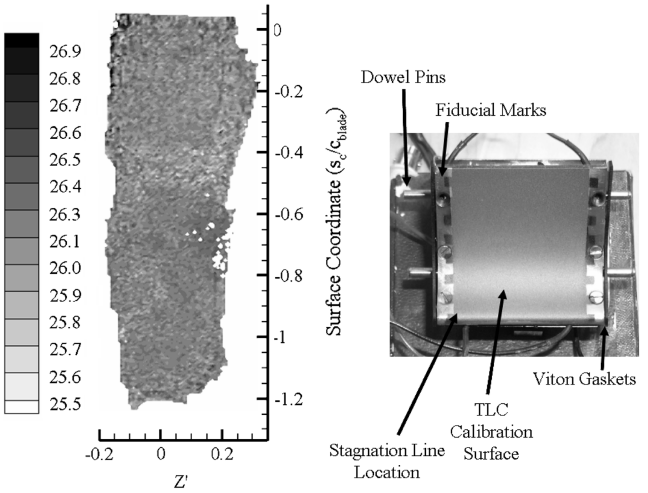

Fig. 5 Sample spatially resolved temperature map (at $T_{set} = 26.2°C$) and TLC-painted copper calibrator surface for comparison.

C. Film Cooling Test Surfaces

We constructed two RenShape pressure-surface measurement surfaces with a conformal constant heat flux surface epoxied onto the airfoil shape. No heat flux was applied to either surface in these experiments. The first (undrilled) surface was used to perform recovery temperature measurements (T_{rec}). Each measured surface consisted of a 25-μm-thick Kapton film coated with 90 Å vacuum-deposited layers of chromium and gold. The choice of material and thickness was the result of extensive experimentation directed toward ensuring that the gold layer uniformly adhered to the substrate material (chromium and Kapton) and provided a uniform heat release. Furthermore, the Kapton film thickness was chosen to ensure that conduction in the streamwise direction could be neglected. This can be estimated by combining the convection and axial conduction thermal resistances to obtain an effective *Biot number* for the gold and Kapton layers that was much greater than 1: $Bi = h(s_{c,\max})^2/kt \gg 1$. The Biot number for the gold layer was estimated to be $1(10)^5$ and $1(10)^6$ for the Kapton layer. The film was wrapped around the leading edge and extended a few millimeters into the bleed chamber.

Figure 6 displays a side view of the completed pressure-surface constant heat flux surface. Note that the film had to bend around a very small radius of curvature (1.27 mm), which eliminated the use of thin metallic foils, as used by Giel et al. [17]. Photographs of this surface with and without the constant heat flux surface are shown in Fig. 7. This figure shows the completed surface painted with liquid crystals and installed in the single-passage model. Five type-K 36-gauge thermocouples were installed at the centerline of each measurement surface to quantify the conductive heat flux into the RenShape substrate. These were embedded a perpendicular distance $\mathcal{P}/c_{blade} = 0.140$ beneath the pressure surface. The *Biot number* for the RenShape surface was found to have a value that was much larger than unity ($Bi = h\mathcal{P}/k \approx 51$). This suggested that both surfaces could be considered adiabatic.

Two rows of compound-angle film cooling holes were installed in the cooled surface. Table 2 summarizes the compound-angle round-hole geometry installed in the pressure surface of the airfoil. The local M_{is} value shown in this table was extracted from the computed distribution presented in Fig. 3. The middle hole of each row coincided with the passage centerline and the number of holes was designed such that the row spanned the distance $-\frac{1}{3} \le Z' \le \frac{1}{3}$. The

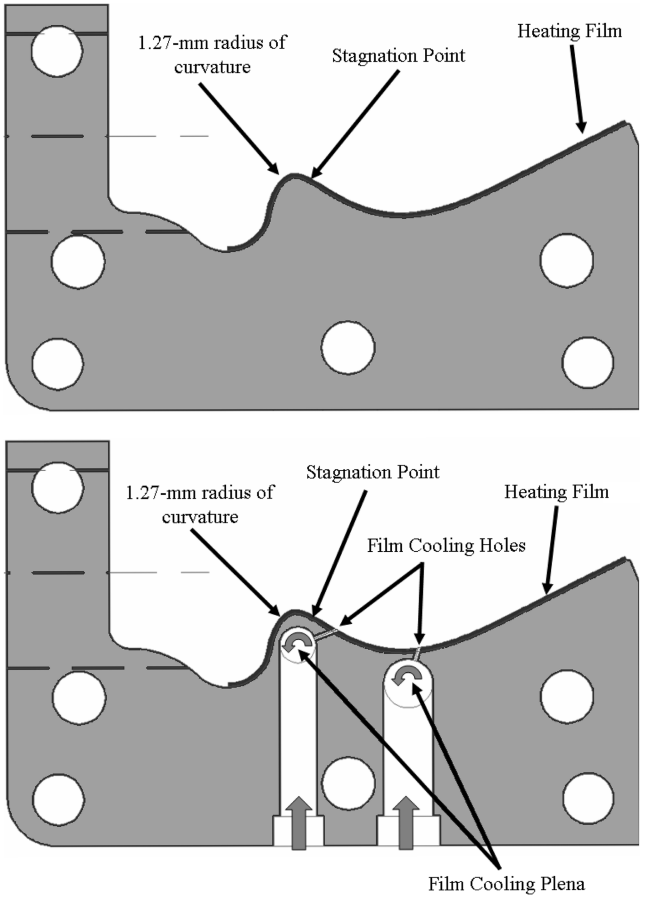

Fig. 6 Schematic of assembled heat flux surface.

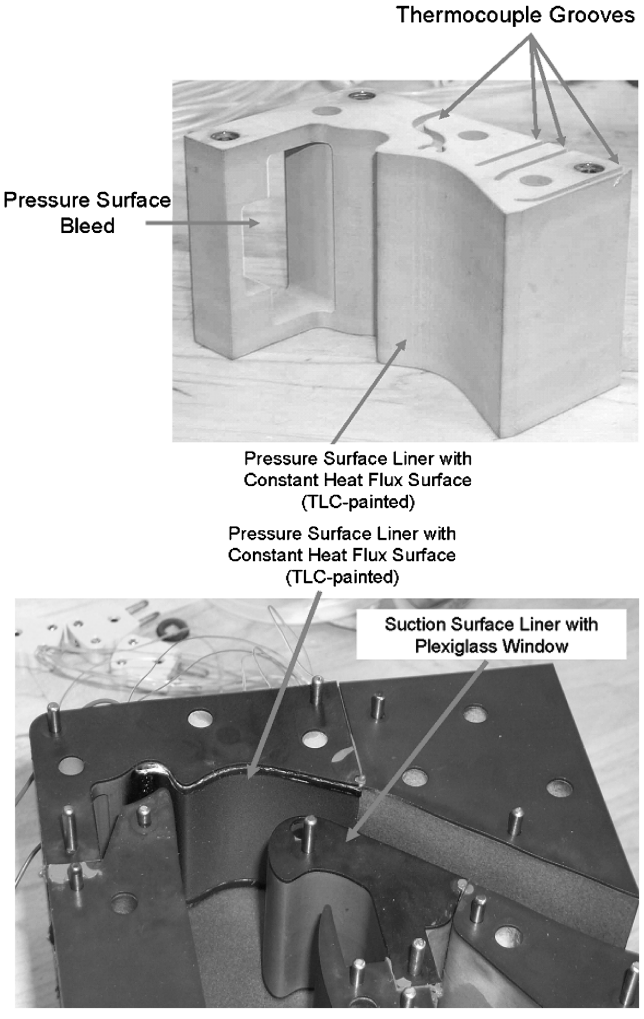

Fig. 7 Photographs of pressure surface with and without constant heat flux surface.

Table 2 Film cooling hole geometry

Row	1	2
Number of holes	17	25
s_c/c_{blade}	−0.110	−0.427
M_{is}	0.067	0.156
α	38.39°	47.81°
β	52.00°	65.00°
p/d	5.29	3.53
L/d	6.03	3.05
Pinned diameter d, mm	0.4293	0.4293
$\dot{m}_j = (\rho u)_j A_{fc,j}$ at BL = 1 kg/s	$1.01(10)^{-5}$	$2.36(10)^{-5}$

cross-sectional areas of the film cooling plena were at least four times the total exit area of the film cooling holes [20]. This resulted in ratios of plenum to film cooling hole diameter of $d/D_{c,1} = 0.094$ and $d/D_{c,2} = 0.070$. The plena consisted of two equal-diameter cross-drilled holes, with the supply at the centerline of the measurement piece. Figure 6 displays side views of the completed pressure-surface measurement surfaces. The coolant stagnation temperature $T_{\circ,j}$ and pressure $P_{\circ,j}$ were measured during testing.

D. Data Reduction and Measurement Uncertainty

This section discusses the various parameters of interest and how they were calculated from measured quantities and their uncertainties. Each test condition was parameterized by the blowing ratio BL, density ratio DR, and momentum ratio I. BL was computed by normalizing the coolant mass flux by the mainstream flux. The freestream static pressure and temperature at the exit of the film cooling hole with no injection were used to compute the mainstream mass flux. The mass flux through each film cooling hole was computed assuming equal mass flow through each film cooling hole. The uncertainties in the blowing ratio for rows 1 and 2 were estimated to be $\delta \text{BL}_1/\text{BL}_1 = 4.0\%$ $(P = 0.95)$ and $\delta \text{BL}_2/\text{BL}_2 = 5.4\%$ $(P = 0.95)$. The density ratio DR is defined using the stagnation pressure and temperature in the film cooling plenum. The uncertainty in this parameter was less than 1%. The momentum ratio was computed by normalizing the mainstream momentum flux $\rho_\infty u_\infty^2$ by the jet momentum flux $\rho_j u_j^2$. The mainstream momentum flux was computed using the static pressure and temperature at the hole exit with no injection, and the jet momentum flux was computed using isentropic flow functions. The uncertainty in this parameter was estimated to be nearly identical to that for the blowing ratio:

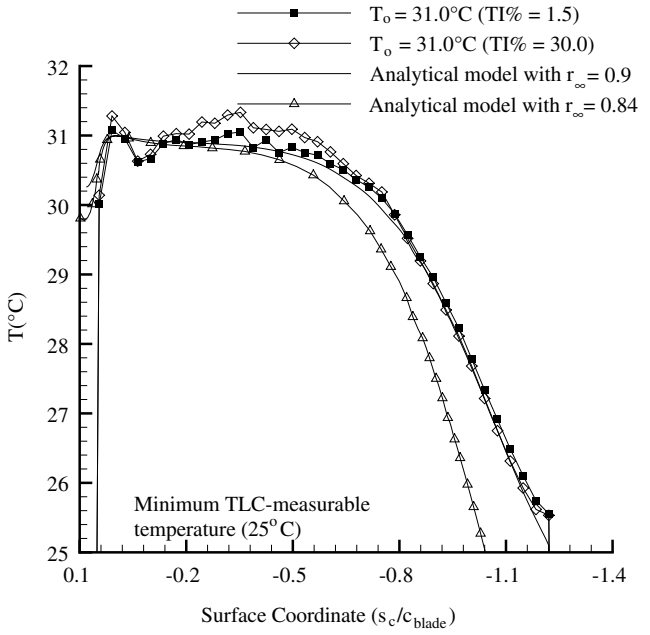

Fig. 8 Measured spanwise-averaged $\bar{T}_{\text{rec}}$ distributions for low- and high-turbulence cases with $T_\circ = 31.0°\text{C}$.

Table 3 Nominal dimensionless-parameter values for T_c blowing-ratio-effect measurements

Case	BL_1	BL_2	I_1	I_2	DR_1	DR_2
1	0.761	0.908	0.599	0.821	1.002	1.012
2	1.080	0.919	1.172	0.808	0.998	1.008
3	1.600	0.956	2.528	0.873	1.005	1.015
4	2.018	1.081	3.988	1.782	1.036	1.047
5	2.911	2.016	7.500	3.440	1.114	1.125
6	5.193	3.420	17.919	7.878	1.464	1.478
7	5.256	5.715	18.439	15.132	1.440	1.454

Table 4 Nominal dimensionless-parameter values for T_c density-ratio-effect measurements

Case	BL_1	BL_2	I_1	I_2	DR_1	DR_2
1	2.497	1.265	3.961	1.131	1.619	1.635
2	3.908	2.569	7.907	3.559	1.825	1.843
3	6.491	4.248	17.688	7.841	2.185	2.206
4	6.422	6.959	18.960	14.265	2.213	2.235

$\delta I_1/I_1 = 4.0\%$ $(P = 0.95)$ and $\delta I_2/I_2 = 5.4\%$ $(P = 0.95)$. All data will be presented using the following definition of the film effectiveness:

$$\eta_T = \frac{T_c - T_{\text{rec}}}{T_{\circ,j} - T_{\text{rec}}} \tag{2}$$

We chose this definition for data presentation because the coolant stagnation temperature was directly measured and did not vary between rows. Drost and Bölcs [4] used this definition as well. T_{rec} was calculated at every position using standard analytical relations with a recovery factor of 0.9. This approach was validated by direct measurements, as we discuss in the Results and Discussion section. The measurement uncertainty of T_{rec} was conservatively estimated to be $\delta T_{\text{rec}} \approx \pm 0.2°\text{C}$. This uncertainty band allowed us to consider the undrilled surface as adiabatic. The film effectiveness experiments were run by heating the coolant to a higher stagnation temperature and measuring T_c. $T_{\circ,j}$ was generally 12°C higher than $T_{\circ,\infty}$. This was experimentally found to be the largest possible temperature difference with acceptable conduction errors. Mukerji and Eaton [21] found that this approach was more convenient in facilities that operate at near ambient conditions. Furthermore, Goldstein [3] and Sinha et al. [22] found that this inverse heat transfer problem is functionally identical to the case in which $T_{\circ,j} < T_{\circ,\infty}$.

The film cooling plena were installed relatively close to the measurement surface (with minimum distances relative to the measurement surfaces of $\mathcal{P}_1/c_{\text{blade}} \approx 0.042$ and $\mathcal{P}_2/c_{\text{blade}} \approx 0.026$). Thus, conductive heat transfer between the plena and the measurement surface was a concern. Nevertheless, estimates of the surface heat flux computed from the backloss thermocouples showed that the resulting estimated uncertainty in the measured T_c distributions was $\delta T_c \approx \pm 0.17°\text{C}$. Using this value and estimated coolant temperature uncertainty of $\delta T_{\circ,j} \approx 0.2°\text{C}$, we estimate a maximum uncertainty in η_T of $\eta \approx 0.01$ using the techniques discussed by Moffat [23] and Kline and McClintock [24]. These uncertainty values match those quoted in previous investigations after accounting for conduction effects [6,22,25]. This is consistent with the fact that the uncertainty of our TLC system relative to the coolant to reference temperature difference, $\delta T/(T_{\circ,j} - T_{\text{rec}}) \approx 2\%$ is identical to previous investigations as well. It is important to note that larger temperature differences would increase δT_c via conduction losses and offset any reduction in $\delta\eta$.

III. Results and Discussion

The following sections present a summary of key results from this experiment. The parameter values (BL, DR, I, TI%, and ℓ) were

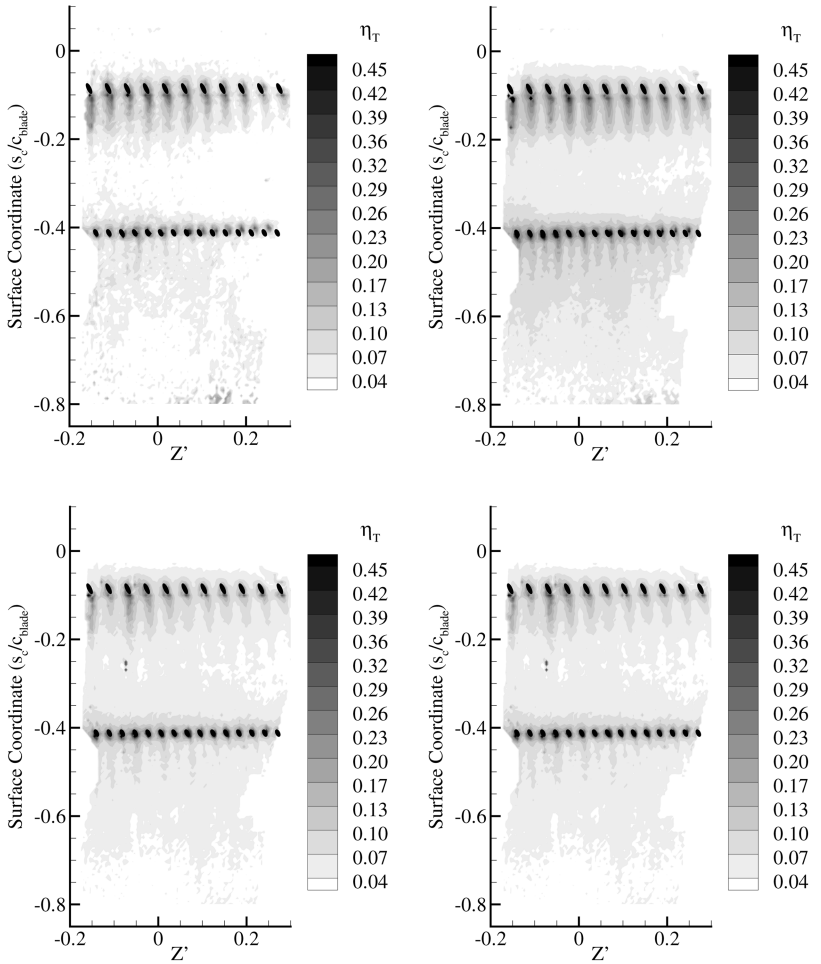

Fig. 9 Spatially resolved maps of η_T showing effects of blowing ratio with fully attached cooling jets; top left: $BL_1 = 0.761$ and $BL_2 = 0.908$, top right: $BL_1 = 1.080$ and $BL_2 = 0.919$, bottom left: $BL_1 = 1.600$ and $BL_2 = 0.956$, and bottom right: $BL_1 = 2.018$ and $BL_2 = 1.081$.

chosen to examine the effects of inlet turbulence, the interaction of the two rows of film cooling holes and the effects of coolant density. All spanwise-averaged measurements consisted of two-dimensional data that were spanwise-averaged over the intersection of the predicted two-dimensional portion of the flow ($-0.25 \leq Z' \leq 0.25$) [11] and the experimentally determined valid viewing area of the miniature periscope system ($-0.12 \leq Z' \leq 0.24$). The mainstream stagnation temperature at the inlet of the blade row was determined by measuring the spanwise-averaged temperature along the measurement surface at its stagnation point.

A. Recovery Temperature Measurements

We acquired recovery temperature data at three distinct values of the total temperature $T_{\circ,\infty}$ with $q'' = 0$. Figure 8 compares the spanwise-averaged, median-filtered recovery temperature $\bar{T}_{\text{rec}}$ to the analytical model with recovery factors of $r = 0.84$ and $r = 0.9$. The first value for r corresponds to the analytical result for laminar flow, $r = Pr^{\frac{1}{2}}$. The $r = 0.9$ value for a fully turbulent boundary layer is taken from Dorrance [26] using a Prandtl number of $Pr = 0.71$. The spanwise-averaged recovery temperature distribution at the low- and high-turbulence cases agree with the turbulent analytical profile within the uncertainty of measured surface temperatures ($\delta\bar{T} \approx \pm 0.17$°C). The correlation coefficient value for the $r = 0.9$ profile was $R^2 = 0.99$, confirming the high quality of the fit. The surface embedded thermocouple measurements confirmed the near-adiabatic nature of the measurement surface. In our report, we compare analytical predictions for surface-temperature profile at three inlet total temperatures $T_{\circ,\infty}$ against spanwise-averaged temperature measurements using the borescope system [27]. The root-mean-squared errors for each set temperature were $|\delta T| \approx$

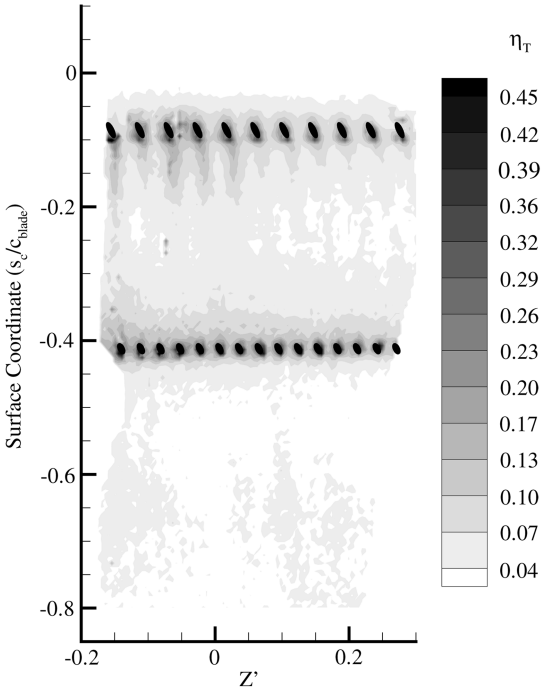

Fig. 10 Spatially resolved map of η_T showing jet liftoff downstream of second row with flow conditions $BL_1 = 2.911$ and $BL_2 = 2.016$.

0.16°C at 27.6°C, 0.22°C at 31.5°C, and 0.17°C at 33.1°C. This gives an overall estimated uncertainty of $|\delta T| \approx 0.19$°C. This result validated the entire TLC measurement approach as it required the disassembly of the model to install the heat transfer measurement surface and repositioning of the miniature periscopes. These data further indicate that the boundary layer is fully turbulent over the aft portion of the airfoil.

B. Effects of Blowing Ratio on Film Effectiveness

Air was used as the coolant for all these cases. Table 3 lists the values for the dimensionless parameters of interest. Note that these values are considerably higher than those previously studied at transonic flow conditions with compound-angle round holes [28,29]. Despite the use of air, the density ratio had a maximum value of DR ≈ 1.45 for the highest blowing ratio cases. Figures 9 and 10 present spatially resolved maps of the film effectiveness based on the coolant stagnation temperature (η_T) for cases in which the cooling jets are attached. There was some uncertainty in the film cooling hole positions shown in the plot ($\delta(s_c/c_{\text{blade}}) \pm 0.02$) due to the repeatability of the periscope positioning. Figure 11 displays the corresponding spanwise-averaged film effectiveness $\bar{\eta}_T$ for all studied cases. The vertical lines correspond to the location of the two rows of film cooling holes. The peak value of η_T directly behind the first row of holes was measured to be $\eta_T \approx 0.3$ and $\eta_T \approx 0.4$ for the second row at the flow condition, $[\text{BL}_1, \text{BL}_2] = [0.761, 0.908]$. These values were insensitive to changes in the blowing ratio.

The general trends presented here are consistent with experience derived from low-speed experiments. The maps of η_T show clear footprints downstream of each hole in the first row. As similar behavior is not observed downstream of the second row, we concluded that this was the result of a higher degree of lateral mixing downstream of this row. This argument was supported by experimental data presented by Ramsey and Goldstein [30] and Lee et al. [31] that showed decreased lateral mixing with decreasing values of α. Hence, the cooling jets maintain their structure over a longer streamwise distance. As the blowing ratio of the first row is increased, with the second approximately constant ($[\text{BL}_1, \text{BL}_2] = [0.761, 0.908], [1.080, 0.919]$) the footprints downstream of the first row of film cooling holes become more distinct and lengthen, consistent with observations reported by Baldauf et al. [32]. An unexpected result was the improvement downstream of the second row of holes as the first row blowing ratio was increased from $\text{BL}_1 = 0.761$ to 1.080. However, Afejuku et al. [33] reported using dual-row incompressible experimental data that film cooling jets produce momentum deficits or excesses that have decisive effects on downstream rows. Momentum excesses were experimentally shown in this report to improve film-layer coverage and limit lateral mixing. We considered this to be the most likely explanation.

Further increases in the first row blowing ratio ($[\text{BL}_1, \text{BL}_2] = [1.600, 0.956]$ to $[2.018, 1.081]$) led to a decrease in the film effectiveness for both rows. Bons et al. [34] reported that the film cooling jets cause increased turbulence levels that convect downstream. Pietrzyk et al. [35] using inclined holes with $\delta_1/d \ll 1$ showed that turbulence intensity levels as high as TI% = 26% can be achieved immediately downstream of a row of holes. Thus, we concluded that the observed degradation was due to increased turbulent mixing. When the blowing ratios of both rows were increased to $[\text{BL}_1, \text{BL}_2] = [2.911, 2.016]$ no further degradation downstream of the first row of film cooling holes was observed in the spanwise-averaged effectiveness $\bar{\eta}_T$ curves shown in Fig. 11. This result was unexpected. However, these data also show that the second row of film cooling jets detach and reattach downstream. On these bases, we concluded that the second row jets detached at a momentum ratio of $I_2 \approx 3.4$ ($\text{BL}_2 \approx 2$). In the case of the first row,

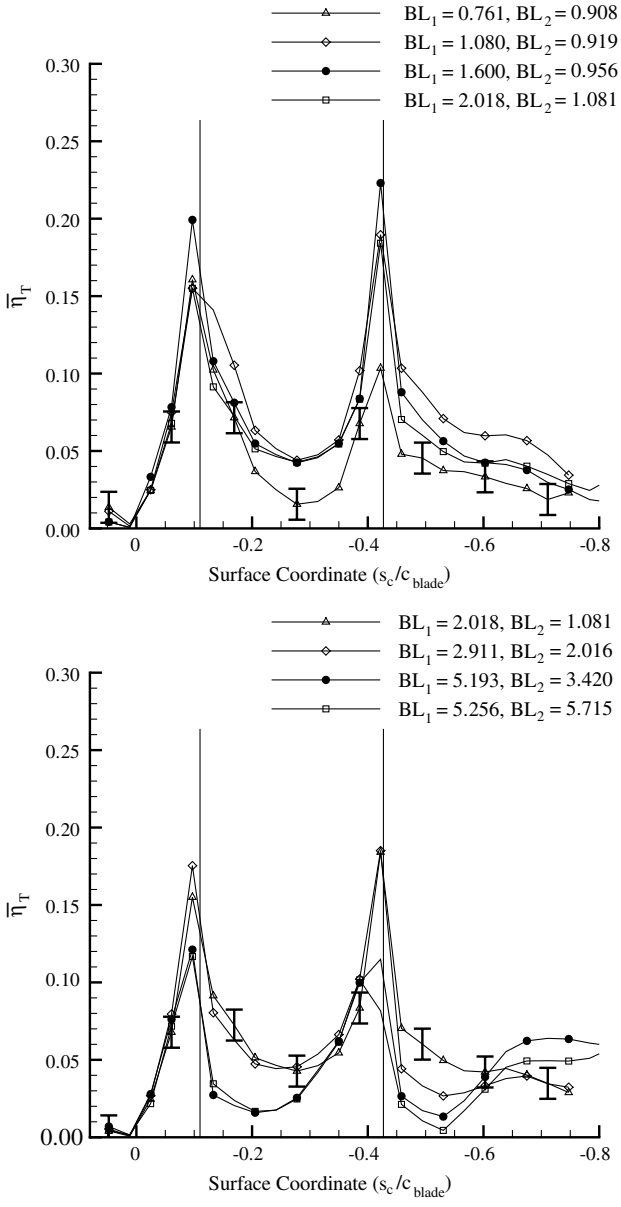

Fig. 11 Plots of $\bar{\eta}_T$ showing the effect of blowing ratio.

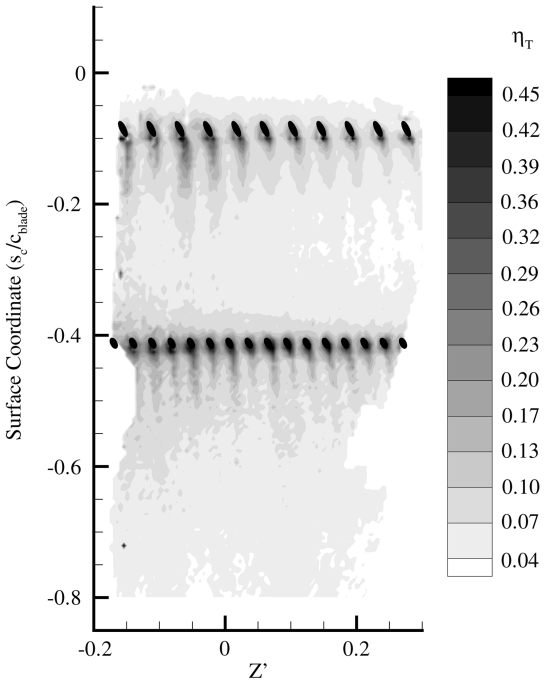

Fig. 12 Spatially resolved map of η_T showing effects of density ratio. Flow condition: $[\text{BL}_1, \text{BL}_2] = (2.497, 1.265)$.

the cooling jets appear to totally blow off from the measurement surface at a blowing ratio of $BL_1 \approx 5$ ($I_1 \approx 18$). This was considerably higher than our expectations from previous studies [22,32]. The spanwise-averaged $\bar{\eta}_T$ curves show a reattachment of the first row of film cooling jets upstream of the second row of holes. Data reported by Bergeles et al. [36] suggest that this reattachment was due to the jets from the first row interacting with the second row of jets.

C. Density Ratio Effects

Table 4 presents the dimensionless parameters of interest for cases in which carbon dioxide is used as the coolant. Figure 12 presents spatially resolved η_T measurements for a representative case with blowing ratios of $[BL_1, BL_2] = (2.497, 1.265)$. The peak values of η_T directly behind each row of holes were measured to be $\eta_T \approx 0.4$ and ≈ 0.5, respectively. Figure 13 compares the spanwise-averaged film effectiveness $\bar{\eta}_T$, with carbon dioxide and air used as coolant. This figure shows that for the $[BL_1, BL_2] = (2.497, 1.265)$ case in which I_1 matches the $[BL_1, BL_2] = (2.018, 1.081)$ air-cooled case, the corresponding values of $\bar{\eta}_T$ were identical. Improved spanwise-averaged effectiveness values were observed downstream of the second row of holes with the carbon dioxide injectant case. This observation is consistent with incompressible flat-plate data reported by Sinha et al. [22], as the momentum ratio for the second row of holes was lower for the carbon dioxide case. Conversely, the subsequent $[BL_1, BL_2] = (3.908, 2.569)$ carbon-dioxide-cooled case has slightly higher momentum ratios than the air-cooled case $[BL_1, BL_2] = (2.911, 2.016)$. Thus, we expect reduced spanwise-averaged effectiveness values. This effect was indeed noted downstream of the first row of holes, where the cooling jets were attached. However, this feature was not observed downstream of the second row of holes, where the cooling jets detached and then reattached downstream. For this condition, improved effectiveness was measured for the carbon-dioxide-coolant case. This result suggests an interaction effect between the two rows of holes.

Figure 13 also shows that the cooling jets from both rows completely lifted off from the measurement surface in the blowing ratio ranges $4 < BL_1 < 6.5$ and $1.3 < BL_2 < 2.5$. It is important to note that this point of jet detachment is in the same range as the air-cooled cases. This observation is particularly interesting as previous investigations indicated that denser jets require higher BL values for jet liftoff. Of particular interest were the high-blowing cases $[BL_1, BL_2] = (6.491, 4.248)$ and $[BL_1, BL_2] = (6.422, 6.959)$ and the matching air-coolant cases $[BL_1, BL_2] = (5.193, 3.420)$ and $[BL_1, BL_2] = (5.256, 5.715)$. The spanwise-averaged data from these data readily collapsed on each other, except for the $[BL_1, BL_2] = (5.193, 3.420)$ air-coolant case, where the measured $\bar{\eta}_T$ values were slightly larger once the cooling jets reattached downstream of the second row of holes. This demonstrated that the choice of coolant was irrelevant once the jets completely detach from the surface.

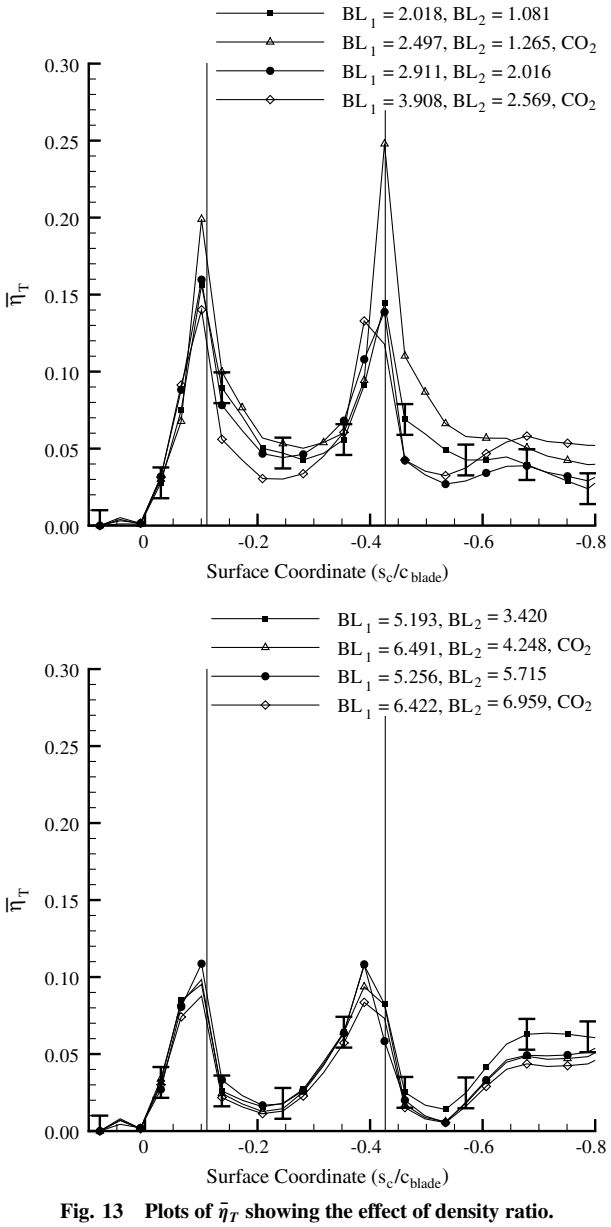

Fig. 13 Plots of $\bar{\eta}_T$ showing the effect of density ratio.

D. Turbulence Effects on Film Effectiveness

Table 5 presents the values for the key parameters of interest for each flow condition. Both carbon dioxide and air were used as the coolant in these cases. Incompressible data reported by Jumper et al. [37] and Bons et al. [34] showed that increased turbulence levels lead to rapid coolant degradation and increased spanwise mixing, especially when the jets are attached to the cooled surface. When the jets are detached from the surface, Bons et al. [34] reported earlier jet reattachment and improved downstream performance. Figure 14 presents a map of η_T taken at the high-turbulence condition with air coolant and blowing ratios of $[BL_1, BL_2] = (2.333, 1.122)$. This figure should be compared against the $[BL_1, BL_2] = (2.018, 1.081)$

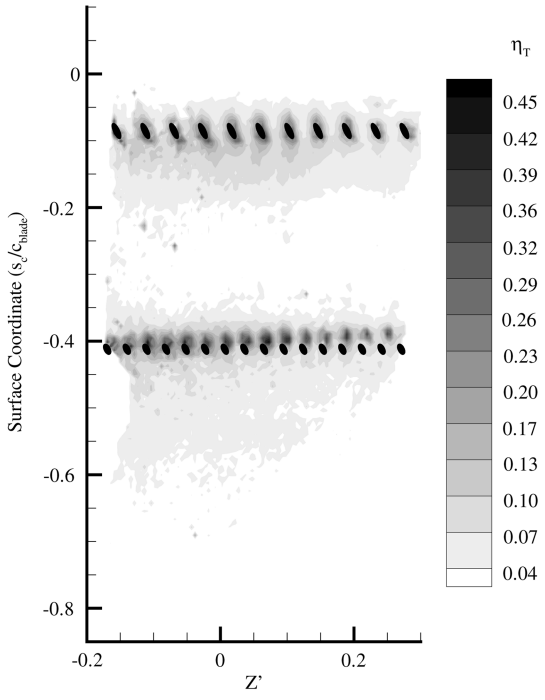

Fig. 14 Spatially resolved map of η_T showing effects of turbulence conditions. Flow condition: $[BL_1, BL_2] = (2.333, 1.122)$.

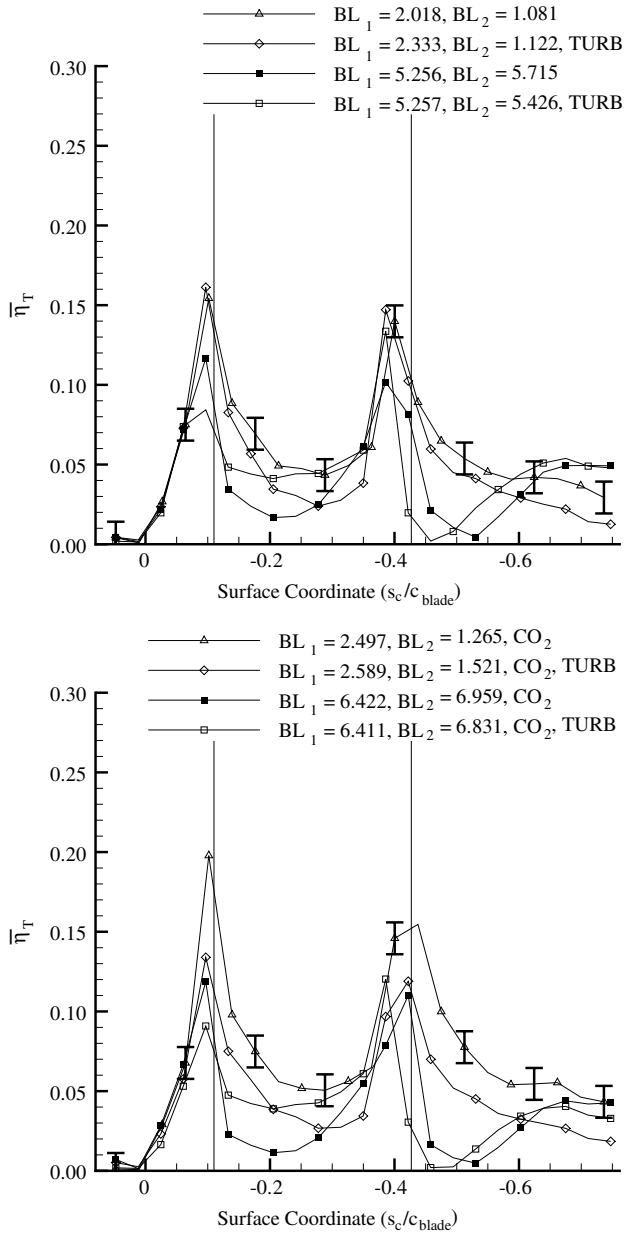

Fig. 15 Plots of $\bar{\eta}_T$ showing the effect of turbulence conditions.

case shown in Fig. 9. This demonstrates that the increased mainstream turbulence intensity TI% caused greatly enhanced mixing. This washed away the cooling footprints downstream of each hole. Additionally, the peak values of η_T immediately downstream of the film cooling hole were reduced to $\eta_T \approx 0.25$ and ≈ 0.3, respectively.

Figure 15 compares the spanwise-averaged film effectiveness $\bar{\eta}_T$ for the cases listed in Table 5 with the corresponding cases presented earlier in this paper. The top part of this figure presents cases in which air was used as the coolant, the bottom half of the figure shows cases in which carbon dioxide was used. These measurements generally show trends that are consistent with data reported by Bons et al. [34] that when the jets are attached to the surface increased values of TI% lead to poorer effectiveness with faster decay rates. Conversely, when the jets are detached, increased values of TI% lead to earlier reattachment and improved performance. This observation was independent of the choice of coolant. As these results are consistent with incompressible data sets, it suggests that the effect of compressibility may be neutralized by higher inlet turbulence levels.

Table 5 Nominal dimensionless-parameter values for T_c turbulence-effect measurements

Case	BL_1	BL_2	I_1	I_2	DR_1	DR_2
1	2.333	1.122	3.869	1.122	1.022	1.032
2	5.257	5.426	18.125	14.516	1.434	1.448
3	2.589	1.521	3.435	1.463	1.633	1.649
4	6.411	6.831	17.411	14.247	2.235	2.256

IV. Conclusions

We have presented measurements of the steady-state film effectiveness for two rows of compound-angle round holes on the pressure surface of a transonic rotor blade. BL, DR, and TI% were higher than in previous investigations on transonic airfoils with coolant ejection. We used high-accuracy thermochromic liquid-crystal thermography to collect film effectiveness data on a verifiable near-adiabatic surface. Accounting for thermal losses due to conduction from the coolant plena, this was experimentally found to have a validated uncertainty of ± 0.2°C. Such accuracy was necessary due to the relatively small $T_{w2} - T_{\text{rec}}$ temperature differences that were necessary to minimize conduction losses. With these preparations, we achieved maximum film effectiveness uncertainties of $\delta\eta = 0.01$. Furthermore, we found that spanwise-averaged data collected at the same nominal blowing conditions collapsed to single curves, suggesting that the uncertainty in η was even lower.

We observed two distinct regimes of film cooling jet-in-crossflow interaction, consistent with previous investigations. One was where the film cooling jet was rapidly entrained into the local boundary layer, the other where the jet blows straight through. Incompressible data predicted a much smaller jet liftoff BL value than observed in this experiment. Clear evidence of the interaction between the two rows of film cooling holes was observed. Denser cooling jets were found to improve the film effectiveness when the cooling jets are attached to the surface. Furthermore, denser jets were found to take longer to be mixed out by the mainstream flow. Surprisingly, these coolant jets had the same effective liftoff BL value. Once the film cooling jets detached, the spanwise-averaged film effectiveness indicated no functional difference between injecting air or carbon dioxide through the film cooling holes. High levels of turbulence were found to rapidly mix out the cooling jets when they were totally attached to the measurement surface. If the coolant jets are detached from the surface, increased turbulence levels encouraged rapid surface reattachment. These conclusions are consistent with incompressible data sets, suggesting that the effect of compressibility is negligible at elevated turbulence levels.

Acknowledgments

This research was sponsored by General Electric Aircraft Engines (GEAE) through their University Strategic Alliance Program. In addition, the first author received support from the National Science Foundation via a three-year Graduate Fellowship. The authors would like to express their sincere gratitude to C. Elkins, D. Mukerji, and A. Vicharelli (at Stanford) and F. Buck, C. Prakash, B. Bergholz, and D. Wisler (at GEAE) for their assistance and advice in the course of this experimental program. Additionally, the authors would like to thank G. Laskowski, G. Medic, C. McNeil, and X. Wu for their support in developing and executing the computational models. L. Johal, S. Sutton, S. Carver, T. Hasler, and J. Glassman are acknowledged for their high level of expertise in machining various parts in this experiment.

References

[1] Medic, G., and Durbin, P., "Toward Improved Film Cooling Prediction," *Journal of Turbomachinery*, Vol. 124, No. 2, 2002, pp. 193–199. doi:10.1115/1.1458021

[2] Kays, W., and Crawford, M., *Convective Heat and Mass Transfer*, 3rd ed., McGraw–Hill, San Francisco, 1993.

[3] Goldstein, R., "Film Cooling," *Advances in Heat Transfer*, Vol. 7, 1971, pp. 321–379.
[4] Drost, U., and Bölcs, A., "Investigation of Detailed Film Cooling Effectiveness and Heat Transfer Distribution on a Gas Turbine Airfoil," *Journal of Turbomachinery*, Vol. 121, No. 2, 1999, pp. 233–242. doi:10.1115/1.2841306
[5] Wang, Z., Ireland, P., and Jones, T., "A Color Image Processing System for Transient Liquid Crystal Heat Transfer Experiments," *Journal of Turbomachinery*, Vol. 118, No. 3, 1996, pp. 421–427.
[6] Drost, U., Bölcs, A., and Hoffs, A., "Utilization of the Transient Liquid Crystal Technique for Film Cooling Effectiveness and Heat Transfer Investigations on a Flat Plate and Turbine Airfoil," American Society of Mechanical Engineers Paper 97-GT-26, 1997.
[7] Haldeman, C., Dunn, M., Barter, J., Green, B., and Bergholz, R., "Aerodynamic and Heat-Flux Measurements with Predictions on a Modern One and One-Half State High Pressure Transonic Turbine," *Journal of Turbomachinery*, Vol. 127, No. 3, 2005, pp. 522–531. doi:10.1115/1.1861916
[8] Vicharelli, A., and Eaton, J., "Turbulence Measurements in a Transonic Two-Passage Turbine Cascade," *Experiments in Fluids*, Vol. 40, No. 6, 2006, pp. 897–917. doi:10.1007/s00348-006-0127-8
[9] Haldeman, C., and Dunn, M., "Heat-Transfer Measurements and Predictions for the Vane and Blade of a Rotating High-Pressure Turbine Stage," *Journal of Turbomachinery*, Vol. 126, No. 1, 2004, pp. 101–109. doi:10.1115/1.1626132
[10] Teekaram, A., Forth, C., and Jones, T., "The Use of Foreign Gas to Simulate the Effect of Density Ratios in Film Cooling," *Journal of Turbomachinery*, Vol. 111, No. 1, 1989, pp. 57–62. doi:10.1115/1.3262237
[11] Kodzwa, P., Laskowski, G., Vicharelli, A., Medic, G., Elkins, C., Eaton, J., and Durbin, P., "Evaluation of Alternatives for 2-D Linear Cascade Facilities," *Journal of Turbomachinery*, Vol. 131, No. 3, 2009, p. 031001. doi:10.1115/1.2985073
[12] Bogard, D., and Thole, K., "Gas Turbine Film Cooling," *Journal of Propulsion and Power*, Vol. 22, No. 2, 2006, pp. 249–270. doi:10.2514/1.18034
[13] Ames, F., "Aspects of Vane Film Cooling with High Turbulence: Part II —Adiabatic Effectiveness," *Journal of Turbomachinery*, Vol. 120, No. 4, 1998, pp. 777–784. doi:10.1115/1.2841789
[14] Chen, Y., and Kim, S., "Computation of Turbulent Flows Using an Extended k-ϵ Turbulence Closure Model," NASA CR-179204, 1987.
[15] Narashima, R., and Sreenivasan, K., "Relaminarization of Fluid Flows," *Advances in Applied Mechanics*, Vol. 19, 1979, pp. 221–309. doi:10.1016/S0065-2156(08)70311-9
[16] Kodzwa, P., and Eaton, J., "Heat Transfer Coefficient Measurements on the Pressure Surface of a Transonic Airfoil," *Experiments in Fluids*, Vol. 48, No. 2, 2010, pp. 185–196. doi:10.1007/s00348-009-0721-7
[17] Giel, P., Boyle, R., and Bunker, R., "Measurements and Predictions of Heat Transfer on Rotor Blades in a Transonic Turbine Cascade," *Journal of Turbomachinery*, Vol. 126, No. 1, 2004, pp. 110–121. doi:10.1115/1.1643383
[18] Kodzwa, P., Elkins, C., Mukerji, D., and Eaton, J., "Thermochromic Liquid Crystal Temperature Measurements Through a Borescope Imaging System," *Experiments in Fluids*, Vol. 43, No. 4, 2007, pp. 475–486. doi:10.1007/s00348-007-0310-6
[19] Kodzwa, P., and Eaton, J., "Angular Effects on Thermochromic Liquid Crystal Thermography," *Experiments in Fluids*, Vol. 43, No. 6, 2007, pp. 929–937. doi:10.1007/s00348-007-0363-6
[20] Buck, F., and Prakash, C., "Design and Evaluation of A Single Passage Test Model To Obtain Turbine Airfoil Film Cooling Effectiveness Data," American Society of Mechanical Engineers Paper 95-GT-19, 1995.
[21] Mukerji, D., and Eaton, J., "Spatially Resolved Measurements of Heat Transfer in Turbomachinery Applications," Stanford Univ., TR TSD-145, Stanford, CA, March 2002.
[22] Sinha, A., Bogard, D., and Crawford, M., "Gas Turbine Film Cooling: Flowfield due to a Second Row of Holes," *Journal of Turbomachinery*, Vol. 113, No. 3, 1991, pp. 450–456. doi:10.1115/1.2927895
[23] Moffat, R., "Describing the Uncertainties in Experimental Results," *Experimental Thermal and Fluid Science*, Vol. 1, No. 1, 1988, pp. 3–17. doi:10.1016/0894-1777(88)90043-X
[24] Kline, S., and McClintock, F., "Describing Uncertainties in Single Sample Experiments," *Mechanical Engineering*, Vol. 75, 1953, pp. 3–8.
[25] Abuaf, N., Bunker, D., and Lee, C., "Heat Transfer and Film Cooling Effectiveness in a Linear Airfoil Cascade," *Journal of Turbomachinery*, Vol. 119, No. 2, 1997, pp. 302–309. doi:10.1115/1.2841113
[26] Dorrance, W., *Viscous Hypersonic Flow*, 1st ed., McGraw–Hill, San Francisco, 1962.
[27] Kodzwa, P., and Eaton, J., "Measurements of Film Cooling Performance in a Transonic Single Passage Model," Stanford Univ., TR TF 93, Stanford, CA, 2005, http://www.stanford.edu/group/fpc/cgi-bin/fpcwiki/Main/Publications [retrieved 2010].
[28] Gauntner, J., "Effects of Film Injection Angle on Turbine Vane Cooling," NASA TP-1095, 1977.
[29] Furukawa, T., and Ligrani, P., "Transonic Film Cooling Effectiveness from Shaped Holes on a Simulated Turbine Airfoil," *Journal of Thermophysics and Heat Transfer*, Vol. 16, No. 2, 2002, pp. 228–237. doi:10.2514/2.6672
[30] Ramsey, J., and Goldstein, R., "Interaction of a Heated Jet with a Deflecting Stream," *Journal of Heat Transfer*, Vol. 93, No. 4, 1971, pp. 365–372.
[31] Lee, S., Lee, S., and Ro, S., "Experimental Study on the Flow Characteristics of Streamwise Inclined Jets in Crossflow on Flat Plate," *Journal of Turbomachinery*, Vol. 116, 1994, pp. 97–105. doi:10.1115/1.2928283
[32] Baldauf, S., Scheurlen, M., Schultz, A., and Wittig, S., "Correlation of Film Cooling Effectiveness From Thermographic Measurements at Enginelike Conditions," *Journal of Turbomachinery*, Vol. 124, No. 4, 2002, pp. 686–698. doi:10.1115/1.1504443
[33] Afejuku, W., Hay, N., and Lampard, D., "Measured Coolant Distributions Downstream of Single and Double Rows of Film Cooling Holes," *Journal of Engineering for Power*, Vol. 105, No. 1, 1983, pp. 172–177. doi:10.1115/1.3227379
[34] Bons, J., MacArthur, C., and Rivir, R., "The Effect of High Free-Stream Turbulence on Film Cooling Effectiveness," *Journal of Turbomachinery*, Vol. 118, No. 4, 1996, pp. 814–825. doi:10.1115/1.2840939
[35] Pietrzyk, J., Bogard, D., and Crawford, M., "Hydrodynamic Measurements of Jets in Crossflow for Gas Turbine Film Cooling Applications," *Journal of Turbomachinery*, Vol. 111, No. 2, 1989, pp. 139–145. doi:10.1115/1.3262248
[36] Bergeles, G., Gosman, A., and Launder, B., "Near-Field Character of a Jet Discharged Normal to a Mainstream," *Journal of Heat Transfer*, Vol. 98, No. 3, 1976, pp. 373–378.
[37] Jumper, G., Elrod, W., and Rivir, R., "Film Cooling Effectiveness in High Turbulence Flow," *Journal of Turbomachinery*, Vol. 113, No. 3, 1991, pp. 479–483. doi:10.1115/1.2927899

K. Frendi
Associate Editor